applied sciences

MDPI

Article

On the Relationship of the Acoustic Properties and the Microscale Geometry of Generic Porous Absorbers †

Tobias P. Ring *,‡ and Sabine C. Langer ‡

TU Braunschweig, Institute for Acoustics, 38106 Braunschweig, Germany

* Correspondence: t.ring@tu-braunschweig.de; Tel.: +49-531-391-8773

† This paper is an extended version of our paper published in Fortschritte der Akustik—DAGA 2021, Wien 2021.

‡ These authors contributed equally to this work.

Abstract: When tailoring porous absorbers in acoustic applications, an appropriate acoustic material model, as well as the relationship between the material model parameters and the microscale geometry of the material, is indispensable. This relationship can be evaluated analytically only for few simple material geometries. Machine-learning models can close this gap for complex materials, but due to their black-box nature, the interpretability of obtained inferences is rather low. Therefore, an existing neural network model that predicts the acoustic properties of a porous material based on the microscale geometry is subject to statistics-based sensitivity analysis. This is conducted to gain insights into the relationship between the microscale geometry and the acoustic material parameters of a generic bar-lattice design porous material. Although it is a common approach in the field of explainable artificial intelligence research, this has not been widely investigated for porous materials yet. By deriving statistics-based sensitivity measures from the neural network model, the explainability and interpretability is increased and insights into the relationship of the acoustic properties and their microscale geometry of the porous specimen can be obtained. The results appear plausible and comparable to existing studies available in the literature, showing if and how the bar-lattice geometry influences the acoustic material parameters. Moreover, it could be shown that the applied global sensitivity analysis method allows us to not only derive a one-to-one parameter impact relation, but also reveals interdependencies that are important to address during a material tailoring process.

Keywords: porous materials; explainable machine learning; neural network; global sensitivity analysis; absorption coefficient; material models; Johnson–Champoux–Allard; inverse parameter identification

Citation: Ring, T.P.; Langer, S.C. On the Relationship of the Acoustic Properties and the Microscale Geometry of Generic Porous Absorbers. *Appl. Sci.* **2022**, *12*, 11066. https://doi.org/10.3390/app122111066

Academic Editor: Roberto Camussi

Received: 30 September 2022
Accepted: 24 October 2022
Published: 1 November 2022

1. Introduction

In recent years, machine-learning-based modeling in engineering applications has taken advantage of the ability to create large amounts of data on the system under investigation using both experimental and numerical approaches. This availability of data allows us to model highly complex systems even without specific knowledge about the underlying physical relations by means of machine-learning approaches; see, e.g., [1]. We state "physical" relations here, since the scope of this paper is on modeling physical systems. However, the statement also applies to every other modeling domain, e.g., social-economic or biological models. Indeed, special approaches also exist that aim to incorporate physical knowledge into machine-learning models, e.g., physics-informed neural networks (PINNs); see, e.g., [2]. Nonetheless, in contrast to physics-based modeling (e.g., applying partial differential equations (PDEs) and solving these numerically), the amount of knowledge about the system under investigation required by machine-learning models is rather low.

1.1. Porous Materials; Applications and Engineering Models

Within this contribution, we focus on the investigation of generic porous materials and their behavior as acoustic absorbers. Porous materials are a well-known measure used to reduce acoustic energy, e.g., as sound absorbers in room acoustics and environmental noise applications [3–5], porous liners in aircraft engines and airframe [6–8] and the reduction of trailing edge noise [9–11], to name a few. Moreover, porous materials can be employed to generate meta-structures and meta-materials. The construction of meta-structures by embedding inclusions into a porous base material is a promising approach to improve the acoustic properties of the base material, as shown in [12,13]. A comprehensive summary of similarities and differences between porous materials and meta-materials is given in [14]. Further recent examples of meta-materials are shown in [15–17]. The widespread applications of porous materials motivates the aim to incorporate them in acoustic simulations. Therefore, material models are required. The material models describing the acoustic behavior of porous materials are hereafter referred to as acoustic models.

In the past, many acoustic models of different complexity for porous materials have been proposed. Starting from the fully empirical models proposed by Delany & Bazley [18] and the subsequent improvement by Miki [19], a range of models based on the idealization of a homogenized material have been established. Therefore, the Biot model [20,21] is the most complex one and is accepted as the reference [22]. The Biot model considers three types of traveling waves in the material: one pressure wave in the fluid phase and one pressure and one shear wave in the solid phase. Accordingly, both the fluid phase and the solid phase (skeleton) of the porous material are assumed to be elastic. Based on the Biot model, several subsequent models have been proposed that assume the solid phase to be rigid, i.e., modeling only one pressure wave in an equivalent fluid. Therefore, the properties of the equivalent fluid also account for the influence of the skeleton on the wave propagation in the fluid phase. These models are accordingly named equivalent fluid models. Well-known models are the Miki model [23], the model of Champoux–Allard [24] and its extensions, the Johnson–Champoux–Allard (JCA) model [25] the Johnson-Champoux–Allard–Lafarge (JCAL) model [26] and the Johnson–Champoux–Pride–Allard–Lafarge (JCPAL) model [27]. All the aforementioned models require a number of model parameters; for the class of equivalent fluid models, these are (a subset of, depending on the specific model) the flow resistivity Ξ, the porosity Φ, the tortuosity α_∞, the thermal and viscous characteristic lengths Λ, Λ', respectively and the static thermal permeability and tortuosity, k_0' and α_0', respectively. It should be noted that in most literature, the flow resistivity is denoted with the symbol σ. For the sake of consistency with our last publications, we choose the letter Ξ here. Additionally, the Biot model requires the elastic parameters of the skeleton phase as well.

1.2. Characterization and Design of Porous Materials

Common to all porous media material models is the aforementioned homogenization. Thus, the models assume a material specimen that is large (in a geometrical sense) in comparison to the material's structure on the microscale. Moreover, the microscale geometry needs to be small compared to the acoustic wavelength [28]. Accordingly, the microscale geometry and, in general, its influence on the parameters of the acoustic model, is taken into account only implicitly when modeling the material. However, this is a major drawback for the goal of tailoring a material to specific needs. Here, tailoring a material is understood as designing and manufacturing a material that exhibits a prescribed behavior, e.g., an absorption coefficient or surface impedance. For tailoring a material, two prerequisites are required: first, the acoustic model parameters and a description of the microscale (for manufacturing purposes) are needed; second, the relationship between these quantities needs to be understood.

The acoustic model parameters can either be measured or obtained by means of inverse parameter identification. The direct measurement is, to the best of the author's knowledge, possible only for the flow resistivity, the porosity and (for electrically non-conductive materi-

als) the tortuosity [28]. By means of inverse parameter identification, the aforementioned parameters, as well as other parameters, can be obtained. Therefore, the material is modeled and, given a specific cost function, e.g., a specified absorption coefficient, the parameters of interest are inversely computed, if required using an optimization algorithm, e.g., see [29–31]. A method capable of recovering all six parameters of the JCAL model from impedance tube measurements is introduced in [32]. On the other side, the microscale geometry of a given porous material can be obtained, e.g., by means of computer tomography (CT) scans, as shown in [33,34]. Additionally, CT scans can support the identification of porous material model parameters when combined with a pore-resolved flow simulation, as shown in [35]. Therefore, a flow simulation of the fluid flow in the pores is conducted using the Lattice-Boltzmann method allowing for a direct computation of flow resistivity, tortuosity and the characteristic lengths. In summation, several approaches exist that allow us to obtain a dataset of the microscale geometry and acoustic model parameters of porous materials, i.e., the first prerequisite for tailoring a porous material.

The second prerequisite, i.e., the relationship between the microscale geometry and the acoustic model parameters, is more challenging. For special microscale geometries, e.g., (slanted) cylindrical pores, the flow resistivity and tortuosity can be derived analytically, as shown in [23]. However, to the best of the author's knowledge, no models exist in the literature that allow us to infer the acoustic model parameters of a given or desired material based on the microscale geometrical parameters for a general material. To circumvent this issue, in a preceding study, we show the application of a machine-learning based approach to model the relation between the microscale geometrical parameters and the acoustic model parameter of a generic porous material [36]. To do so, generic porous material specimens were produced using additive manufacturing, and two different machine-learning models were trained to predict the acoustic model parameters of the JCAL model based on geometrical parameters describing the microscale geometry. The acoustic model parameters were obtained using an inverse parameter identification procedure and the geometrical parameters were known because the materials were manufactured beforehand using additive manufacturing. The resulting machine-learning models were used to close an optimization loop to generate specimens with a desired absorption coefficient.

1.3. Applications of Machine-Learning Methods to Porous Materials

Recently, many approaches have been presented in the literature that employ machine-learning techniques to porous media modeling. Some examples are presented here. In [37], an approach is presented to design an acoustic sink, i.e., a duct-shaped structure filled with porous material, with desired acoustic behavior using a convolutional neural network in an encoder–decoder setting. The acoustic sink is modeled using a combination of transfer matrix method and the JCA model. The authors show that the obtained model is able to derive the geometrical parameters of the acoustic sink for a given absorption spectra, and can predict the absorption spectra for a given set of geometry parameters. In [38], a deep-learning approach is pursued to estimate the parameters for water-saturated porous material from ultrasound tomography data. The authors show the accuracy of the approach, even for a wide range of material parameters. A direct prediction of the absorption coefficient of a layered porous material sample by means of a neural network is shown in [39]. Therefore, the neural network requires only the density and flow resistivity of the porous materials and macroscale geometrical parameters, such as thickness and sequence of the layers. The authors obtain a good agreement with measured absorption coefficients. A similar approach with a sparse amount of input data is presented in [40]. The authors show the use of neural networks to predict the absorption coefficient and surface impedance of porous materials based only on the frequency and the flow resistivity. Although obtaining good results, the authors note that the developed models only suffice for a given class of materials, and do not necessarily have the ability to generalize for other material classes. An application of neural networks for predicting the absorption coefficient of natural fibers is presented in [41]. The authors model the porous material

using a phenomenological approach and with a neural network, and verify better prediction quality of the neural network. An approach concerned with the characterization of porous materials with inclusions using a Gaussian-process-based machine-learning approach is presented in [42,43]. The authors model the porous material using both the model of Delany & Bazley (with the Miki improvement) and the JCA model. It is shown that the improvement introduced by using the JCA model compared to the Delany & Bazley model allows the machine-learning model to reach a better prediction quality along with less training effort. The resulting models are used for predicting the acoustic behavior with regard to the transmission loss.

1.4. Scope, Contribution and Hypothesis of the Study

Although the greatest strength of machine-learning models is to yield system descriptions based on data only, this is another major drawback. Machine-learning models are most often treated as black-box systems. Thus, the rationale behind the obtained predictions remains unclear, and the explainability and interpretability are rather limited [44,45]. This challenge is also apparent for the models obtained in our preceding work [36]. In that study, we produced machine-learning-based models that predicted the acoustic model parameters of the JCAL model for a generic porous material based on the microscale geometry parameters. Although the obtained models appeared to yield acceptable predictions for the acoustic material parameters from the microscale of the porous materials, an interpretation of which microscale parameters affects which acoustic model parameter, and how and why such interaction is observed, could hardly be drawn. In order to further investigate the credibility of the machine-learning models obtained in the preceding study, and to derive insights into the underlying physics that are coded in the machine-learning models, here, the machine-learning models are subjected to a thorough sensitivity analysis. This approach is common in the field of explainable artificial intelligence ('XAI') [46] and, although testing the sensitivity of the prediction rather than the prediction itself is a limitation, the approach is accepted to support the understanding of the inferences of black-box machine-learning models [45,47,48].

As mentioned in the previous section, machine-learning is already quite common in acoustics in general, and specifically in modeling porous materials. However, to the best of the authors' knowledge, no attempts to increase the explainability of machine-leaning models applied to porous materials are available in the literature. Thus, the scope of this contribution is the explainability of machine-learning models for porous materials. Building on the preceding study by the authors [36], the goal of this study is to derive insights into the underlying physics of generic porous materials coded in the machine-learning models. Therefore, the sensitivity of the outputs of the machine-learning models, i.e., the acoustic model parameters, with respect to the inputs, i.e., the microscale geometry of the porous material, is investigated. The hypothesis of this contribution is as follows: the relationships of the acoustic model parameters and the material's microscale can be modeled using machine-learning approaches, and can be investigated by applying statistics-based sensitivity analysis to the resulting machine-learning model.

The presented study should be viewed as a natural follow-up of our previous paper on designing generic porous materials using machine-learning approaches [36]. Moreover, the presented paper is an extension of a prior conference contribution (German only) [49].

1.5. Outline of the Paper

The outline of the paper is as follows: in Section 2, the tools used within this study are presented. The investigated generic porous specimens are presented in Section 2.1. The inverse parameter identification approach for obtaining the acoustic model parameters is summarized in Section 2.2. The neural network model is presented in Section 2.3 together with an overview of its performance. The approach of the global sensitivity analysis used to derive the insights into the behavior of the neural network model is outlined in Section 2.4. The results of the study are presented in Section 3 with the results for the first-order

and total sensitivity measures in Section 3.1 and for the the second-order coefficients in Section 3.2. The results are discussed and compared to results in the literature in Section 4. A brief summary is given in Section 5.

2. Materials and Methods

Within this section, the investigated generic porous materials are described, as well as the experimental and numerical tools for their characterization. Moreover, the statistical methods and the machine-learning model used to investigate the relations between the model parameters and the material's microscale geometry are presented. This contribution is a follow-up of a preceding paper [36]; thus, for the sake of completeness, Section 2.1 summarizes the generation of the generic porous media investigated here and Section 2.2 summarizes the inverse parameter identification process. Although these sections contain results, the content is not largely different from the former study [36]: therefore, the content is placed here within this "Materials and Methods" section in order to not confuse it with the findings of this present study. In the following sections, the methods specific to this study are presented; these are the application of an artificial neural network used to model the relationship between geometry variables and acoustic model parameters, as described in Section 2.3. It should be noted here that in the preceding study, a neural network model was employed as well, but the model used here is slightly improved in structure and accuracy, and thus is presented here again. Finally, the approach of the global sensitivity analysis is described in Section 2.4.

2.1. Design of Generic Porous Media Samples

Within this contribution, generic porous media are investigated that are designed using a simple bar-lattice design. The general design is shown in Figure 1a. The specimen have a circular shape with a diameter of 30 mm. The specimen thickness l is 15 mm. These quantities are kept constant within this contribution. The inner geometry is determined by a certain number of layers stacked upon each other, each layer consisting of a lattice of parallel bars. The geometry of each bar is determined by the bar width d and the bar height h. The bars of each layer are spaced by the bar spacing s. Moreover, from one layer to the next (direction bottom-up), each bar lattice is turned by the plane angle φ. The variables d, h, s, φ are hereafter referred to as design variables, since they fully determine the microscale geometry of the specimen. A photograph of one sample is shown in Figure 1b. The specimens are produced using additive manufacturing (also known as 3D-printing). A more detailed description on the manufacturing of the specimen can be found in [36].

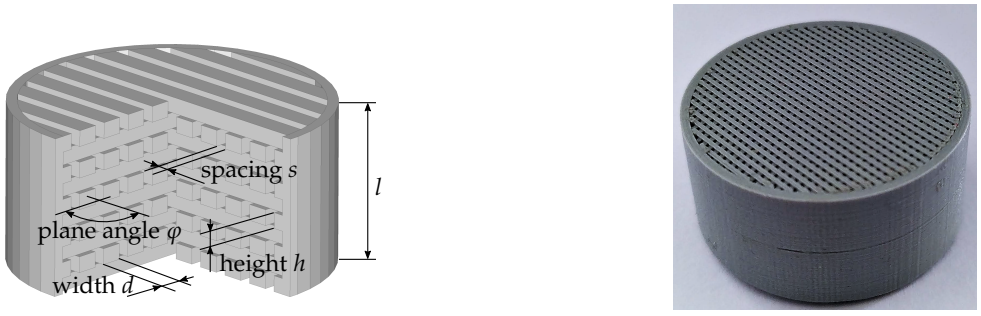

(**a**) (**b**)

Figure 1. Photograph and schematic design of the generic porous media samples. (**a**) Design variables used to parameterize the material properties [36]. (**b**) Photograph of a printed generic porous media sample [36].

In order to allow for a machine-learning-based modeling of the relation between the specimen microscale and the resulting porous media model parameters, a Latin-

Hypercube Sampling (LHS) of the design variables is conducted using the parameter ranges given in Table 1.

Table 1. Parameter ranges of the design variables for the LHS [36].

Bar Width (d)	Bar Spacing (s)	Bar Height (h)	Plane Angle (φ)
0.10–0.50 mm	0.10–1.00 mm	0.05–0.20 mm	0–90°

Based on the LHS-procedure and the parameter ranges given in Table 1, a set of 50 specimens is produced. These fill the parameter space, and thus exhibit various acoustic properties. In order to generate the input data required for the inverse parameter identification described in Section 2.2, the parameters flow resistivity Ξ and absorption coefficient α of all specimens are measured. The flow resistivity is measured using the alternating flow method based on ISO 9053-2 [50], and the absorption coefficient is measured using the two-microphone technique in an impedance tube based on ISO 10543-2 [51] in the frequency range of 900–6600 Hz. For more details on the measurement, the reader is asked to refer to our preceding contribution [36]. Figure 2 shows the measured flow resistivity (Figure 2a) and the measured absorption coefficient (Figure 2b) of all specimen.

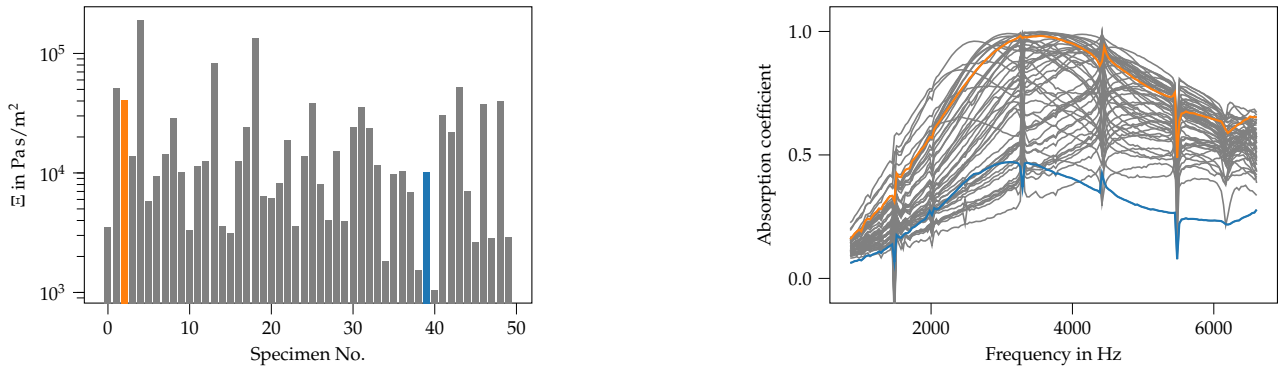

(**a**) (**b**)

Figure 2. Measurement results of all 50 test specimen. The specimen with the highest mean absorption coefficient is marked in orange. The specimen with the lowest mean absorption coefficient is marked in blue. (**a**) Flow resistivity measurement results of all specimen. The flow resistivity was measured using the alternating flow method [36]. (**b**) Absorption coefficient measurement results of all specimen. The absorption coefficient was measured in an impedance tube using the two-microphone technique [36].

In Figure 2, the measurement results of all specimens are shown in gray color, while two are colored separately. The sample with the highest mean absorption coefficient is marked in orange (specimen no. 2, counting 0–49); the sample with the lowest mean absorption coefficient (specimen no. 39) is marked in blue. These samples are seen as somewhat extreme samples regarding the absorption coefficient. However, it can be verified from the results of the flow resistivity that these specimens do not show extreme values for this quantity. Thus, the flow resistivity cannot serve as the only explanatory variable for the general behavior of the material with regard to the absorption coefficient. This finding motivates the approach to model the relation between the model parameters and the microscale geometry using machine-learning. It is expected that a machine-learning model—here, specifically, a neural network—can model the (expected) nonlinear relationship between the microscale geometry and the acoustic model parameters and can be trained based on the available experimental data. Therefore, an inverse parameter identification procedure is pursued to extract the acoustic model parameters based on the measured quantities flow resistivity and absorption coefficient. This is described in the following section.

2.2. Inverse Parameter Identification of the Acoustic Model Parameters

For the modeling of the porous material within this study, the JCA model is used. It is a five-parameter model, with the model parameters flow resistivity Ξ, porosity Φ, the tortuosity α_∞ and the viscous and thermal characteristic lengths Λ, Λ'. Within the preceding study, the Johnson–Champoux–Allard–Lafarge (JCAL) model was used that adds the static thermal permeability k_0' as a sixth parameter. However, during preliminary tests for this contribution it was observed that the JCA model reaches an acceptable representation of the measurements results as well. Moreover, in another study available in the literature, this model is applied for a very similar generic and additively manufactured porous material as well [52]. However, the three-parameter Miki model was observed to not reach an acceptable representation of the material behavior. Therefore, here, the (compared to the JCAL model) slightly simpler JCA model is used. Since the model parameters cannot be measured directly (with the methods available to the authors), an inverse parameter identification procedure is used to determine the parameters Φ, α_∞ and Λ, Λ'. The flow resistivity Ξ is measured, and can thus be used as an input parameter to the inverse procedure.

As already mentioned, the procedure is completely described in the preceding contribution [36], and thus is summarized here. The inverse procedure is based on modeling the effect of the porous material as an equivalent fluid using the JCA model in front of an impervious and rigid wall under plane wave loading. This setting resembles the measurement of the absorption coefficient in the impedance tube. Using this model, the absorption coefficient for a given set of model parameters can be predicted. A genetic algorithm is used to adjust the model parameters, such that the error between the measured absorption coefficient (see Figure 2b) and the absorption coefficient predicted by the model is minimized. Therefore, the differences for all measured/predicted frequencies are weighted equally, and the error is reported as the sum of squared differences. The flow resistivity, as obtained from the measurement, remains unchanged during the optimization process. Finally, the model parameters that fit the measurement best are obtained. This procedure is undergone ten times for each specimen. Since the genetic algorithm that is used for the parameter identification is of stochastic nature, the obtained results differ slightly from run to run. Thus, data augmentation is achieved, since for all inputs (the geometry parameters), a set of ten slightly different model parameters are obtained. In total, a dataset comprising 500 pairs of geometry values and JCA model parameters is obtained. However, it should be noted that these parameters only represent a best fit, and therefore are not necessarily physically correct. In order to investigate the general validity of the resulting parameters, a plausibility check for the porosity is shown in the preceding study [36]. For the investigated generic porous specimens, the porosity can be calculated approximately based on the bar geometry by $\Phi \approx \frac{s}{s+d}$. These results are compared to the parameter values resulting from the optimization process, and are in reasonable agreement with the analytic prediction. Thus, it is assumed that the parameter values resulting from the optimization process are a reasonable estimate of the correct physical values.

2.3. Modeling the Relation of JCA Model Parameters and Microscale Geometry Using an Artificial Neural Network

After the inverse parameter identification, for each specimen, the geometry parameters (from manufacturing) and the corresponding JCA model parameters are known. Between these sets, a model f, mapping the four geometry parameters $\boldsymbol{X}$ to the five model parameters $\boldsymbol{Y}$, is built:

$$\begin{aligned} \boldsymbol{Y} &= f(\boldsymbol{X}) \\ f &: \mathbb{R}^4 \rightarrow \mathbb{R}^5 \quad . \end{aligned} \tag{1}$$

The model f is built within this contribution using an artificial neural network (ANN), using the keras/tensorflow library [53]. A "classic" structure as a densely connected feed-

forward neural network with three hidden layers is used. All layers use the Rectified Linear Unit (ReLU) activation function. The input data are scaled to the unit interval before being presented to the network. The final structure of the network is found in a trial-and-error approach. Since the resulting network is very similar to the one presented in [36], the reader is referred to that study for more details on the network. The network has a total of 1,111,721 parameters and is trained using the Adam algorithm and the "mean squared error" error measure. The results are reported using the coefficient of determination R^2. The model can be seen schematically in Figure 3.

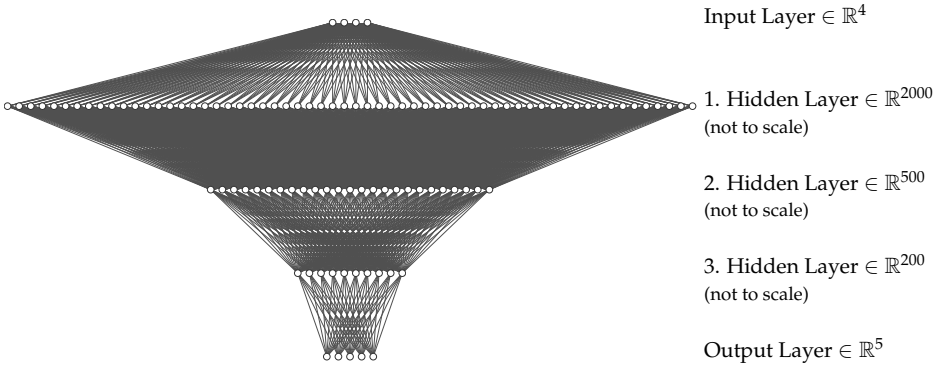

Figure 3. The artificial neural network used within this contribution. The size of the hidden layers is not to scale.

The available dataset is split into three parts, namely the training set, the validation set and the test set. The test dataset amounts to 20 % of the data, and is not used for the training and model generation. The remaining 80 % of the data are used in a threefold cross-validation. Thus, the model is trained using two-thirds of the data (the training dataset) and is tested against the remaining one-third (validation dataset). This training procedure is repeated using different model structures. The best results have been obtained with the model shown in Figure 3.

Hereafter, a short overview of the model performance is given. Since no general changes are made and only slight accuracy improvements are achieved compared to the preceding study, the results of the performance evaluation are shown in this section. The training score of this model is $R^2 = 0.83 \pm 0.12$, whereas the reported uncertainty accounts for twice the standard deviation ($\approx$95 % confidence interval) and is computed over the three cross-validation runs. The model is finally evaluated using the (yet unseen) test dataset, resulting in a test score of $R^2 = 0.93$. The increase in the test score relative to the training score here results from an increase in available training data, as the model is retrained using the entire training and validation dataset before computing the test score. The ability of the model to predict the JCA model parameters from the geometry values is shown using correlation plots in Figure 4. In the plots, the prediction of the ANN with the geometry values from the test dataset as input is shown in the vertical axis. The horizontal axis shows the correct model parameter that corresponds to the geometry parameter taken by the ANN. It can be seen that the correlation is good for the flow resistivity and acceptable for the remaining parameters.

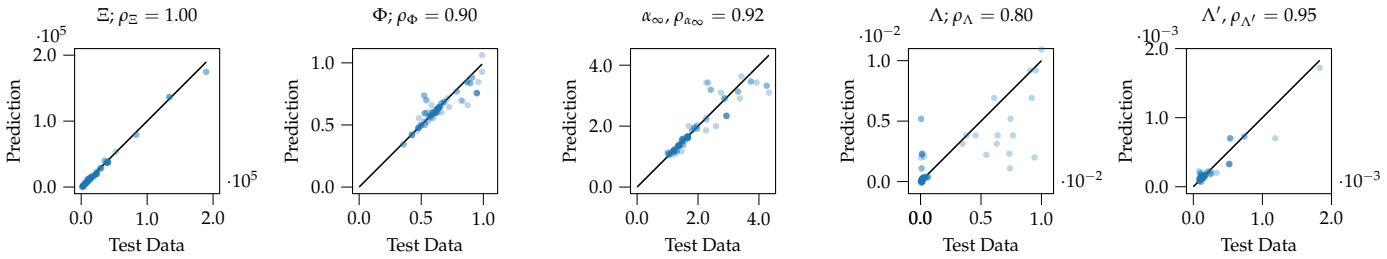

Figure 4. Correlations of correct model parameters (input to the ANN) and the prediction of the ANN. The data shown are the test dataset only (unseen data during training). The correlation is measured using Pearson's correlation coefficient ρ. Greek letters denote the JCA model parameters, i.e., Ξ: flow resistivity, Φ: porosity, α_∞: tortuosity, Λ, Λ′: viscous and thermal characteristic length, respectively.

2.4. Global Sensitivity Analysis

The machine-learning model introduced in Section 2.3 is used to model the relation of the JCA model parameters and the microscale geometry of the additively manufactured specimens—here, the design variables. In order to gain insight about the underlying physics, the machine-learning model is analyzed using global sensitivity analysis (GSA). Within this section, a summary of the mathematical descriptions of the sensitivity measures is given. In-depth information about GSA can be found in various literature; here, mainly the textbook [54] should be mentioned. All the following information on GSA is based on this reference.

The sensitivity c_i of an arbitrary function g regarding its inputs $\boldsymbol{Z} = \{z_1, \ldots, z_i, \ldots, z_n\}$ can be seen as its derivatives with regard to the inputs, i.e.,:

$$c_i = \left. \frac{\partial g}{\partial z_i} \right|_{z_i}. \tag{2}$$

This procedure is often referred to as one-factor or one-at-a-time sensitivity analysis, and is based on the first-order second moment approach [55]. The partial derivative in Equation (2) can be computed in a non-intrusive way using a parameter variation and applying finite differences. However, the procedure has (at least) two major drawbacks. Being a first-order method, the relation for the sensitivity given in Equation (2) is a linear approximation. Thus, for general (nonlinear) functions g, the resulting sensitivity measure is only valid in the proximity of the nominal value of z_i. Another drawback is that interdependencies of the input variables for not purely additive functions g cannot be accounted for.

A more general and realistic sensitivity measure can be computed using the approach of the GSA. Thereby, the sensitivity is measured by the amount of variance in the output quantity that is caused by the variance of each input quantity. Since the input variance is a global measure in the sense that the amount of variance accounts for the entire input range that each z_i can take, the value of the output variance is also accounting for the entire input range, and thus, sensitivity measures valid for the entire parameter range are obtained. Additionally, the influence of interdependencies of the inputs can be measured to some extend.

In order to evaluate the sensitivity of the model output regarding its inputs, a statistical approach is used. Following a Monte Carlo Simulation of the model, the variance of the output $\mathbb{V}(Y)$ and the variance of the conditional expectation of the model with regard to the input $\mathbb{V}(\mathbb{E}(Y|X_i))$ are measured. With these quantities, the sensitivity coefficient of the model regarding its i-th input can be computed using:

$$S_i = \frac{\mathbb{V}(\mathbb{E}(Y|X_i))}{\mathbb{V}(Y)}. \tag{3}$$

The sensitivity coefficients S_i are referred to as first-order effects, and measure the main effect of the i-th input quantity on the model output. It should be noted that, for purely additive models, all first-order effects add up to one, i.e.,:

$$\sum_i S_i = 1. \tag{4}$$

The first-order effects account for the direct (main) effect of the i-th input quantity on the model output. However, there can be interaction effects: for example, simultaneous changes of two input quantities may compensate or amplify each other. Such effects cannot be accounted for by a simple one-at-a-time sensitivity analysis. However, the framework of the GSA allows for the measurement of such effects using the interaction effects S_{ij}. To account for the influence of interactions, the variance of the output quantity $\mathbb{V}(Y)$ is decomposed into the contributions of its inputs and their combinations:

$$\mathbb{V}(Y) = \sum_i \mathbb{V}(X_i) + \sum_i \sum_{j>i} \mathbb{V}\big(X_i, X_j\big) + \ldots + \mathbb{V}(X_{123\ldots k}). \tag{5}$$

Thus, the variance of the model is accounted for as the sum of the variance contributions of single inputs (main effects, first term in Equation (5)) and the variance cause by higher-order effects. The variance due to second-order effects $\mathbb{V}\big(X_i, X_j\big)$ then reads

$$V_{ij} = \mathbb{V}\big(X_i, X_j\big) = \mathbb{V}\big(\mathbb{E}\big(Y|X_i, X_j\big)\big) - \mathbb{V}(\mathbb{E}(Y|X_i)) - \mathbb{V}\big(\mathbb{E}\big(Y|X_j\big)\big), \tag{6}$$

and by dividing Equation (6) by the overall variance of the model $\mathbb{V}(Y)$, the second-order effect $S_{ij} = \frac{V_{ij}}{V}$ can be computed:

$$S_{ij} = \frac{\mathbb{V}\big(\mathbb{E}\big(Y|X_i, X_j\big)\big)}{\mathbb{V}(Y)} - S_i - S_j. \tag{7}$$

Whereas Equation (4) holds only for purely additive models (i.e., those that have no interaction effects), a similar relation can be written for general models by dividing Equation (5) by the overall variance $\mathbb{V}(Y)$:

$$1 = \sum_i S_i + \sum_i \sum_{j>i} S_{ij} + \ldots + S_{123\ldots k}, \tag{8}$$

implying that for a general model, all main and interaction effects add up to one. Next to the main and interaction effects, the so-called total effects can be computed, which combine the main effect and all interaction effects for each input quantity X_i. To compute the total effect for each input quantity, the idea is to compute the amount of variance in the model output that cannot be attributed to the input quantity under investigation and compared to the overall variance with all inputs. This yields the following form for the i-th total sensitivity index S_{T_i}:

$$S_{T_i} = 1 - \frac{\mathbb{V}(\mathbb{E}(Y|\boldsymbol{X}_{\sim i}))}{\mathbb{V}(Y)} \tag{9}$$

with $\mathbb{E}(Y|\boldsymbol{X}_{\sim i})$ denoting the conditional expectation of the output given all inputs except from the i-th input quantity. It should be noted that generally $\sum_i S_{T_i} \geq 1$, since here, the interaction effects of all inputs are counted multiple times, i.e., in all corresponding interactions. An efficient method to compute the aforementioned sensitivity indices is presented e.g., in [56].

Within this study, the *SALib* implementation in python is used [57] for the necessary computations with respect to the GSA. The underlying Monte Carlo procedure employs a Quasi Monte Carlo approach with a Sobol sequence [58] for equal sampling of the parameter space. A total of $1 \cdot 10^6$ Monte Carlo runs is performed. Since the used python framework assumes a scalar valued model output, the analysis is performed for each output separately.

However, since all inputs are processed in parallel, this is assumed to not limit the applied method. The parameter bounds for all inputs $\boldsymbol{X}$ used according to Table 1 and scaled to a uniform distribution $\boldsymbol{X} \sim \mathcal{U}(0,1)$.

3. Results

The results of the GSA with all inputs and for all outputs are shown below. In Section 3.1 the results for the main effect and total effect of all inputs are shown; the results for the second-order effect are shown in Section 3.2.

3.1. First Order and Total Sensitivity Coefficients

The GSA results for the main effects and total effects are shown in Figure 5. In Figure 5a the first-order effects of the four design variables bar width d, bar height h, bar spacing s and plane angle φ are plotted for all output quantities. It can be seen that even the highest effect (bar width d on tortuosity α_∞) is rather low (less than 0.50). This indicates that strong interaction effects are present and that the underlying model function found by the ANN is nonlinear.

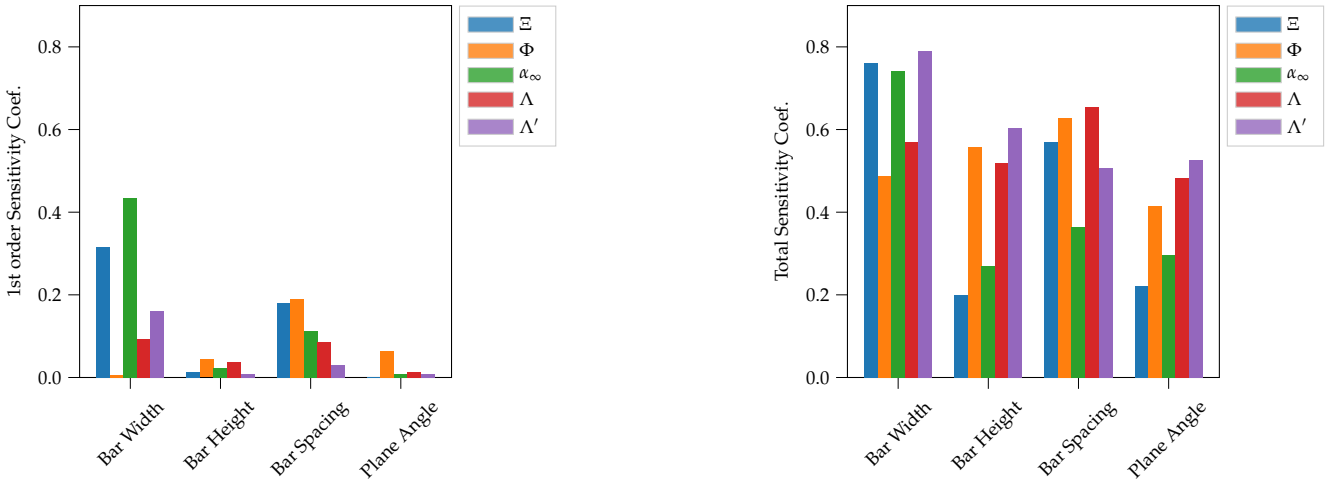

(**a**) (**b**)

Figure 5. First order and total sensitivity coefficients of the microscale geometry parameters of the porous material with respect to the JCA model parameters. Results reported after $1 \cdot 10^6$ Monte Carlo runs (Quasi Monte Carlo with Sobol sequence). The Greek letters denote the JCA model parameters, i.e., Ξ: flow resistivity, Φ: porosity, α_∞: tortuosity, Λ, Λ′: viscous and thermal characteristic length, respectively. (**a**) First-order sensitivity coefficients. (**b**) Total sensitivity coefficients.

Apart from the finding of an expected nonlinearity, the results in Figure 5a are not easy to interpret. However, it can be stated that the bar width and bar spacing have the largest influence on the flow resistivity, and the bar width has a strong effect on tortuosity. Both findings seem reasonable: the influence of the bar width and bar spacing on the flow resistivity can be explained with a blocking of the open area, thus blocking the fluid that flows through the material. An increase in bar width should increase the flow resistivity, while an increase in the spacing should reduce the flow resistivity. However, both effects might compensate each other when happening simultaneously. This interaction indeed is found using the second-order effects and is discussed in the following Section 3.2. Moreover, the main effect of the bar width on tortuosity seems explainable, too: as the bar width increases while the other geometry parameters remain unchanged (first order effect), the streamline of a fluid particle becomes longer in contrast with a small bar width. This is illustrated in Figure 6.

Figure 6 schematically shows a cut through two specimen with different bar widths. The specimens are cut perpendicular to the bars in the first, third and fifth layer (accordingly: parallel to the bars in the second and fourth layer). A plane angle of 90° is assumed,

i.e., the bars are perpendicular from one layer to the next. The bar spacing and bar height are identical in Figure 6a,b, respectively. In blue, a possible fluid streamline is shown. It can be seen that the path is longer in Figure 6a; thus, an increase in the bar width increases the tortuosity. A similar description can be found in [59]. There, the authors conduct flow computations using the Lattice–Boltzmann method on several generic porous structures, including a U-shaped channel. From the computed flow fields, the tortuosity is estimated. The authors show that the tortuosity of such U-shaped channel scales approximately with $\alpha_\infty \sim 1 + \frac{2}{L}b$ with b denoting the depth of the U-shape and L being the overall length of the channel in the flow direction. Since in this study, the sensitivity is investigated, a comparison between the cases should employ the derivative of the given formula with respect to b, i.e., $\frac{\partial \alpha_\infty}{\partial b} \sim \frac{2}{L}$. Thus, the tortuosity scales positively and linearly with the depth of the U-shaped channel. Applying the geometry description used in this study, the depth of the U-shaped b is the analogue to the bar width d, the length of the channel L in the direction of propagation is analogue to the bar height h. Thus, an increase in bar width d results in an increased tortuosity. In summary, the observed influence of the bar width on the tortuosity seems plausible.

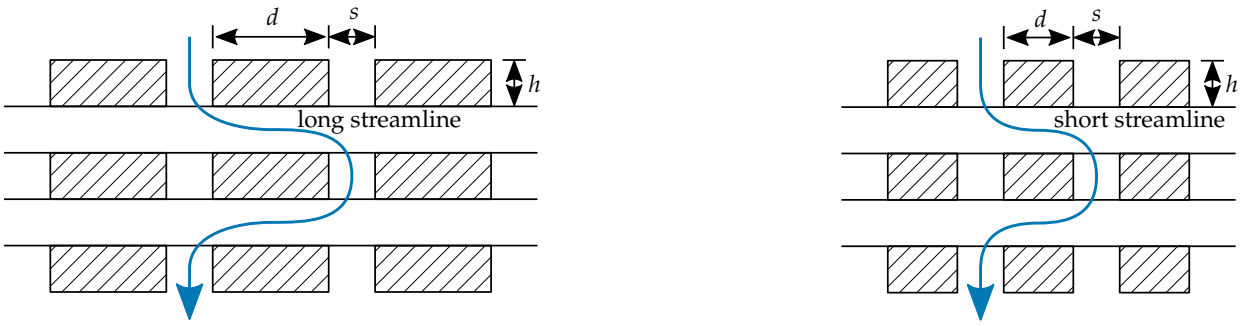

(**a**) (**b**)

Figure 6. An illustration of how the bar width could effect tortuosity. The bar width d is changed; bar height h and spacing s remain unchanged. The blue arrows show a possible streamline of a fluid particle. The length of the streamline positively correlates with the apparent tortuosity. (**a**) Fluid streamline for a large bar width and thus rather long streamline. (**b**) Fluid streamline for a small bar width, and thus, rather short streamline.

Similar to the first-order effects, the total sensitivity coefficients are shown in Figure 5b. The magnitude of the sensitivity values is generally larger than the first-order sensitivity coefficients. This is reasonable, since the total sensitivity coefficients account for both the first-order effect, as well as the higher-order (interaction) effects. Here, the bar width also has the largest effect on most parameters; these are the flow resistivity, the tortuosity and the viscous characteristic length. Large effects are also observed for the bar spacing. This is similar to the findings for the first-order sensitivity coefficients. The lowest effects (on average) are shown for the plane angle.

In summary, an analysis of the first-order and total sensitivity coefficients offers an important insight into the effects of the microscale geometry on the model parameters. Moreover, the relations found seem reasonable. However, these findings only show the effects of single parameters. Interdependencies, if apparent, cannot be found, or are only implicitly contained in the total effects. For the case shown here, rather large differences between first-order and total sensitivity coefficients are apparent, indicating that strong interaction effects influence the behavior. Therefore, an analysis of the second-order effects can help us to investigate the behavior further. This is shown in the next section.

3.2. Second-Order Effects

A deeper insight into the dependencies between the different design variables can be gained by evaluating the second-order effects. The second-order effects measure the combined influence of two input quantities which are not explainable by one quantity

alone. Figure 7 shows the computed second-order effects for each output quantity in matrix form. Bright colors indicate a large effect, while dark colors indicate a small effect.

The leftmost matrix shows the interaction effects for the flow resistivity Ξ. By inspecting the colorbar, it can be seen that the effects are generally smaller than the main effects (compare Figure 5a), as the largest value is approx. 0.20 for the *d*-*s* (bar width–bar spacing) interaction. This interaction effect seems intuitive, as both quantities are found to have an effect on the flow resistivity on their own; see Figure 5a. Moreover, they exhibit an interaction effect that is similarly large as the effect of the bar spacing alone. This can be explained as follows: an increase in the bar width increases the flow resistivity, while an increase in the bar spacing decreases the flow resistivity when both parameters are investigated on their own. Both effects together can either compensate or amplify each other; thus, the interaction effect is important, too. The remaining interaction effects are rather low compared to the *s*-*d*-interaction, and thus are not discussed any further here.

The second left plot shows the interaction effects on the porosity. In general, it can be verified that the magnitude is lower than the one for the flow resistivity, with a maximum of approx. 0.10. Here, the bar width d and bar height h together have the largest effect. This result is counter-intuitive for the following reason. As mentioned before, the porosity of the generic specimen can be roughly estimated by $\Phi = \frac{s}{s+d}$; thus, the bar height is not expected to have a major influence on the porosity. However, the mentioned formula does not account for the effect that an increased bar height reduces the total number of bar planes in the specimen. This might influence the apparent tortuosity for the entire specimen as well. Therefore, this observed interaction effect does not seem implausible.

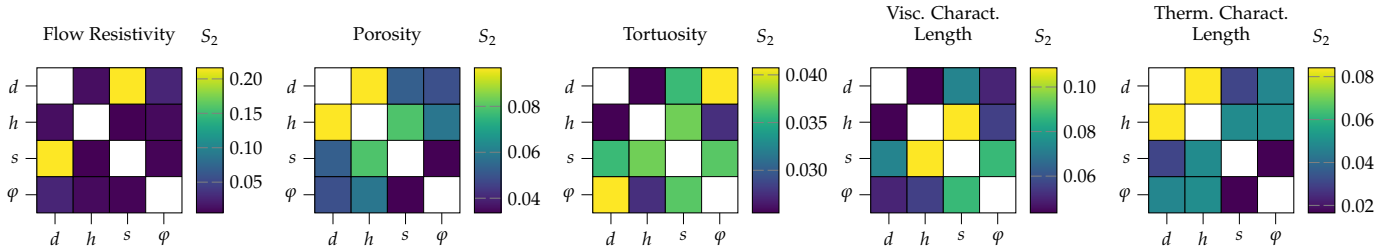

Figure 7. Second-order sensitivity coefficients of the porous material. The letters denote the geometry parameters as: d: bar width, h: bar height, s: bar spacing, φ: plane angle.

The matrix shown in the middle of Figure 7 displays the second-order effects for the tortuosity. Generally, it can be seen that the magnitude of the effects for this model parameter are the lowest of all investigated parameters. The most important interaction effect is found for the parameters bar width d and plane angle φ. This could be explained as follows: for the first-order sensitivity index for the bar width d, a large impact on the tortuosity could be already verified and explained, cf. Figure 6, for a plane angle φ of 90°. For other plane angles smaller than 90°, the bars perpendicular to the drawing plane in Figure 6 become slanted. Thus, the path segment for the fluid particle with horizontal movement in Figure 6 is even longer; thus, the tortuosity should be smallest for a plane angle of 90°. This results in a compensating effect when the bar width is increased but the plane angle decreases. Thus, the d–φ second-order effect accounts for this interaction. With the d-φ interaction having the largest effect, other interaction effects can be verified in this plot as well, e.g., $s - h$, $s - \varphi$ with an impact of approx. 0.037 and $s - d$ width and approximate value of 0.035.

The fourth and fifth matrix plots in Figure 7 show the interaction effects for the viscous and thermal characteristic lengths, Λ, Λ', respectively. The interaction effects for these parameters are of similar magnitude and show one salient interaction each. This is the interaction of the bar height h and the bar spacing s for the viscous characteristic length and the interaction between the bar width d and the bar height h for the thermal characteristic length. Although specific interactions of the geometric parameters relevant

for the characteristic length can be verified, no clear explanation can be given here. For instance, in [24] the definition for the thermal characteristic length is given as

$$\Lambda' = 2\,\frac{\int_V dV}{\int_A dA} \quad , \tag{10}$$

with the pore volume V and the pore surface A. Based on the simple approximation that the pores in each bar plane are the voids between two adjacent bars, the volume and surface of these voids depend on the bar spacing s and the bar height h. However, the bar spacing does not appear to be relevant in the interaction found for the thermal characteristic length, which is d–h. Rather, this interaction effect is verified for the viscous characteristic length. This could be explained as follows: in [28] the relation $\Lambda' = 2\Lambda$ is given for fibrous materials with a porosity close to one. Thus, both lengths depend linearly on each other, and thus, similar interaction effect might occur for both lengths. However, it should be noted that the porosity assumption mentioned in [28] is not verified here (the porosity of the generic specimen is at the magnitude of 0.50) and that the underlying physical relations for these lengths might be somewhat different. Thus, to properly explain the interactions observed for both, the viscous thermal characteristic lengths, a more complex model for the apparent pore geometry seems to be required.

4. Discussion

In Section 3.1 the results for the first-order and total sensitivity coefficients for the microscale geometry parameters (bar width d, bar spacing s, bar height h, plane angle φ) with respect to the acoustic model parameters (flow resistivity Ξ, porosity Φ, tortuosity α_∞, viscous and thermal characteristic lengths Λ, Λ') are presented. The results for the second-order effects are shown in Section 3.2. Generally, the observed direct impacts of the geometrical parameters on the acoustic model parameters as well as interaction effects seem plausible. Next, the findings shown in Section 3 shall be compared to similar investigations available in the literature.

Although, to the best of the author's knowledge, GSA has not been applied yet to explain machine-learning models that model porous materials, it has been applied in [60] to pore-network model descriptions of a complex polyurethane (PU) foam. In that study, the authors describe the foam on the microscale by a set of geometric parameters, among which the mean pore radius $\overline{R_p}$, the mean throat radius $\overline{R_t}$ and the mean frame thickness $\overline{T_f}$ appear to be most comparable to geometry descriptions used in the study presented here. The acoustic properties of the PU foam are described using the JCA model. The authors report the first-order sensitivity index for all JCA model parameters with respect to the microscale geometry of the foam. Although the PU foam is far more complex in shape and random in the geometric distribution, comparable findings to the study presented here are reported by the authors. For instance, the flow resistivity of the PU foam is most influenced by the throat radius and pore radius. Assume that the throat radius, i.e., the radius of the small interconnections between pores of the PU foam, is comparable to the bar spacing, and the pore radius is comparable to the sum of bar spacing and half of the bar width. This analogue is used in a similar way in [61]. With this assumption, it can be verified in Figure 5a that these quantities are the most influential parameters for the flow resistivity in our generic porous materials. However, the relative influence is inverted. For the foam, the pore size has the largest influence and the throat radius ranks second. Here, the bar width has the highest influence and the bar spacing ranks second. This inversion of the influence is probably due to the rather different geometrical nature of the foam and the generic material presented here. Another comparable finding can be verified for the porosity. The most influencial first-order effect regarding the porosity in Figure 5a is the bar spacing. In [60] the authors show that for the PU foam, the porosity is equally influenced by both the throat radius (that is assumed here to be comparable with the bar spacing) and the mean frame thickness. The frame thickness has no direct analogue in our generic material. However, the comparable influence of the bar spacing/the throat thickness on the porosity

can be verified in both studies. A third similarity is the generally large influence of the throat thickness on all studied acoustic model parameters of the PU foam except from the tortuosity. This can be verified for our material as well, as the bar spacing appears to have an impact on all model parameters.

Although not based on sensitivity analysis, from [52], comparable findings can be drawn as well. The authors investigate a generic additively manufactured material very similar to the material we investigated. They also model the material based on the JCA model and derive the JCA model parameters using inverse parameter identification similar to the approach we applied in [30,36]. The authors vary the overall dimensions of the printed specimens measured by the size of the representative elementary volume (REV). Thereby, they simultaneously vary Infill Line Distance (ILD, comparable to the bar spacing) and the Infill Layer Thickness (ILT). Since the authors also use a fused deposition-modeling-based additive manufacturing process, and thus the strands are of nearly circular cross-sectional shape, the ILT is comparable to both the bar width and bar height. The authors report a strong relationship between the size of the REV and both the tortuosity and the flow resistivity. Moreover, a rather weak relationship between the porosity and the REV size is reported. Comparable results can be verified in Figure 5a for the bar width that is similar to the ILT. Here, a strong relation between the bar width and both the flow resistivity and the tortuosity can be verified. Additionally, a relevant influence of the bar spacing, which is similar to the ILD, can be verified. Although the GSA approach used in this study hinders the evaluation of the direction of the influences, the inverse behavior of the flow resistivity and the bar spacing/ILD already presumed in Section 3.1 is verified by the results reported in [52].

In summary, it can be said that the results found in this study are plausible and comparable to other studies available in the literature. The approach of modeling the acoustic model parameters of a generic porous material based on the microscale geometry by means of a machine-learning approach seems feasible. Moreover, the application of sensitivity analysis on the machine-learning model allows the inferences obtained from the machine-learning model to be explained to some extent. To this end, more efficient tailoring of materials might become possible by restricting the parameter optimization to the most physically influential geometry parameters. The approach using the GSA is assumed to be superior over the use of derivative-based sensitivity measures since the entire relevant parameter range is accounted for and deviations due to nonlinearities in the model function are included in the results. Moreover, insights into interaction effects can be gained. Here, the ongoing research in the field of "explainable AI" (AI: artificial intelligence) and its application to porous materials might allow more deep and justified insights into the underlying physics, and thus might allow even more efficient tailoring of materials.

5. Conclusions

Based on an existing machine-learning model that maps the relationship between the microscale geometry and acoustic model parameters of a generic porous material, in this contribution, a statistical analysis of the resulting machine-learning model is conducted. By means of a global sensitivity analysis approach, the major impacts of all geometry variables on the acoustic model parameters are investigated. It is shown that such an approach allows the impacts to be measured quantitatively and ranked. Moreover, parameter interdependencies can be revealed by the employed method. Most observed impacts seem plausible and can be explained; thus, the approach is assumed to deliver reliable results. Comparisons to existing similar approaches in the literature support the validity of the approach. Based on the approach shown here, insights into the behavior of machine-learning models can be gained, and information for their application can be drawn. For the special case of the porous media investigated here, the investigation shows which parameters are most influential for the acoustic model parameters and thus need to be retained for efficiently designing the material, whereas weakly influential parameter might be neglected.

Moreover, interaction effects can be verified. This information could help to further optimize porous materials during a tailoring process, since apparent interdependencies might rule out some optimization procedures and knowledge about highly influential parameters raises the awareness for a required accurate manufacturing process. However, further research is required, since the application of machine-learning models that are solely based on data suffer from the limited explainability of the obtained predictions. Thus, underlying physical effects can be studied only to a limited extent. Methods from the field of explainable artificial intelligence may be able to close this gap.

Author Contributions: Conceptualisation, T.P.R. and S.C.L.; methodology, software, validation, formal analysis, visualisation, T.P.R.; writing—original draft preparation, T.P.R.; writing—review and editing, T.P.R. and S.C.L.; supervision and project administration, S.C.L. All authors have read and agreed to the published version of the manuscript.

Funding: This research received no external funding.

Data Availability Statement: The data presented in this study are available on request from the corresponding author.

Acknowledgments: We acknowledge support by the Open Access Publication Funds of Technische Universität Braunschweig.

Conflicts of Interest: The authors declare no conflicts of interest.

Abbreviations

The following abbreviations are used in this manuscript:

ANN	Artificial Neural Network.
CT	Computer Tomography.
GSA	Global Sensitivity Analysis.
ILD	Infill Line Distance
ILT	Infill Layer Thickness
JCA	Johnson–Champoux–Allard.
JCAL	Johnson–Champoux–Allard–Lafarge.
JCPAL	Johnson–Champoux–Pride–Allard–Lafarge.
LHS	Latin Hypercube Sampling.
PDE	Partial Differential Equation.
PINN	Physics INformed Neural Network.
PU	Polyurethane
ReLU	Rectified Linear Unit.
REV	Representative Elementary Volume.

References

1. Janiesch, C.; Zschech, P.; Heinrich, K. Machine learning and deep learning. *Electron. Mark.* **2021**, *31*, 685–695. [CrossRef]
2. Raissi, M.; Perdikaris, P.; Karniadakis, G.E. Physics-informed neural networks: A deep learning framework for solving forward and inverse problems involving nonlinear partial differential equations. *J. Comput. Phys.* **2019**, *378*, 686–707. [CrossRef]
3. Lázaro, J.; Pereira, M.; Costa, P.A.; Godinho, L. Performance of Low-Height Railway Noise Barriers with Porous Materials. *Appl. Sci.* **2022**, *12*, 2960. [CrossRef]
4. Pereira, M.; Carbajo, J.; Godinho, L.; Ramis, J.; Amado-Mendes, P. Improving the sound absorption behaviour of porous concrete using embedded resonant structures. *J. Build. Eng.* **2021**, *35*, 102015. [CrossRef]
5. Piao, Z.; Heutschi, K.; Pieren, R.; Mikhailenko, P.; Poulikakos, L.D.; Hellweg, S. Environmental trade-offs for using low-noise pavements: Life cycle assessment with noise considerations. *Sci. Total Environ.* **2022**, *842*, 156846. [CrossRef]
6. Beck, S.; Langer, S. Modeling of flow-induced sound in porous materials. *Int. J. Numer. Methods Eng.* **2014**, *98*, 44–58. [CrossRef]
7. Beck, S.C.; Müller, L.; Langer, S.C. Numerical assessment of the vibration control effects of porous liners on an over-the-wing propeller configuration. *Ceas Aeronaut. J.* **2016**, *7*, 275–286. [CrossRef]
8. Teruna, C.; Rego, L.; Avallone, F.; Ragni, D.; Casalino, D. Applications of the Multilayer Porous Medium Modeling Approach for Noise Mitigation. *J. Aerosp. Eng.* **2021**, *34*, 04021074. [CrossRef]
9. Teruna, C.; Avallone, F.; Ragni, D.; Rubio-Carpio, A.; Casalino, D. Numerical analysis of a 3-D printed porous trailing edge for broadband noise reduction. *J. Fluid Mech.* **2021**, *926*, A17. [CrossRef]

10. Rossignol, K.S.; Suryadi, A.; Herr, M.; Schmidt, J.; Tychsen, J. Experimental investigation of porous materials for trailing-edge noise reduction. *Int. J. Aeroacoustics* **2020**, *19*, 365–384. [CrossRef]
11. Herr, M.; Rossignol, K.S.; Delfs, J.; Lippitz, N.; Mößner, M. Specification of porous materials for low-noise trailing-edge applications. In Proceedings of the 20th AIAA/CEAS Aeroacoustics Conference, Atlanta, GA, USA, 16–20 June 2014; p. 3041.
12. Magliacano, D.; Ouisse, M.; Khelif, A.; De Rosa, S.; Franco, F.; Atalla, N. Computation of wave dispersion characteristics in periodic porous materials modeled as equivalent fluids. In Proceedings of the ISMA 2018—International Conference on Noise and Vibration Engineering and USD 2018—International Conference on Uncertainty in Structural Dynamics, Leuven, Belgium, 17–19 September 2018; pp. 4741–4751.
13. Magliacano, D.; Ouisse, M.; De Rosa, S.; Franco, F.; Khelif, A. Investigations about the modelling of acoustic properties of periodic porous materials with the shift cell approach. In Proceedings of the 9th ECCOMAS Thematic Conference on Smart Structures and Materials, SMART 2019, Paris, France, 8–11 July 2019; pp. 1112–1123.
14. Yang, M.; Sheng, P. Sound Absorption Structures: From Porous Media to Acoustic Metamaterials. *Annu. Rev. Mater. Res.* **2017**, *47*, 83–114. [CrossRef]
15. Zhao, H.; Wang, Y.; Yu, D.; Yang, H.; Zhong, J.; Wu, F.; Wen, J. A double porosity material for low frequency sound absorption. *Compos. Struct.* **2020**, *239*, 111978. [CrossRef]
16. Ma, F.; Wang, C.; Du, Y.; Zhu, Z.; Wu, J.H. Enhancing of broadband sound absorption through soft matter. *Mater. Horizons* **2022**, *9*, 653–662. [CrossRef] [PubMed]
17. Li, X.; Yu, X.; Zhai, W. Additively Manufactured Deformation-Recoverable and Broadband Sound-Absorbing Microlattice Inspired by the Concept of Traditional Perforated Panels. *Adv. Mater.* **2021**, *33*, 2104552. [CrossRef] [PubMed]
18. Delany, M.; Bazley, E. Acoustical properties of fibrous absorbent materials. *Appl. Acoust.* **1970**, *3*, 105–116. [CrossRef]
19. Miki, Y. Acoustical properties of porous materials-Modifications of Delany-Bazley models. *J. Acoust. Soc. Jpn.* **1990**, *11*, 19–24. [CrossRef]
20. Biot, M.A. Theory of Propagation of Elastic Waves in a Fluid-Saturated Porous Solid. I. Low-Frequency Range. *J. Acoust. Soc. Am.* **1956**, *28*, 168–178. [CrossRef]
21. Biot, M.A. Theory of Propagation of Elastic Waves in a Fluid-Saturated Porous Solid. II. Higher Frequency Range. *J. Acoust. Soc. Am.* **1956**, *28*, 179–191. [CrossRef]
22. Bolton, J.S.; Kang, Y.J. Elastic porous materials for sound absorption and transmission control. *SAE Trans.* **1997**, 2576–2590.
23. Miki, Y. Acoustical properties of porous materials-generalizations of empirical models. *J. Acoust. Soc. Jpn.* **1990**, *11*, 25–28. [CrossRef]
24. Champoux, Y.; Allard, J. Dynamic tortuosity and bulk modulus in air-saturated porous media. *J. Appl. Phys.* **1991**, *70*, 1975–1979. [CrossRef]
25. Johnson, D.L.; Koplik, J.; Dashen, R. Theory of dynamic permeability and tortuosity in fluid-saturated porous media. *J. Fluid Mech.* **1987**, *176*, 379–402. [CrossRef]
26. Lafarge, D.; Lemarinier, P.; Allard, J.F.; Tarnow, V. Dynamic compressibility of air in porous structures at audible frequencies. *J. Acoust. Soc. Am.* **1997**, *102*, 1995–2006. [CrossRef]
27. Pride, S.R.; Morgan, F.D.; Gangi, A.F. Drag forces of porous-medium acoustics. *Phys. Rev. B* **1993**, *47*, 4964–4978. [CrossRef] [PubMed]
28. Allard, J.; Atalla, N. *Propagation of Sound in Porous Media: Modelling Sound Absorbing Materials 2e*; John Wiley & Sons: Hoboken, NJ, USA, 2009.
29. Atalla, Y.; Panneton, R. Inverse acoustical characterization of open cell porous media using impedance tube measurements. *Can. Acoust.* **2005**, *33*, 11–24.
30. Ring, T.P.; Langer, S.C. Design, Experimental and Numerical Characterization of 3D-Printed Porous Absorbers. *Materials* **2019**, *12*, 3397. [CrossRef]
31. Lippitz, N.; Blech, C.; Langer, S.; Rösler, J. Identification of material parameters for the simulation of acoustic absorption of fouled sintered fiber felts. *Materials* **2016**, *9*, 709. [CrossRef]
32. Jaouen, L.; Gourdon, E.; Glé, P. Estimation of all six parameters of Johnson-Champoux-Allard-Lafarge model for acoustical porous materials from impedance tube measurements. *J. Acoust. Soc. Am.* **2020**, *148*, 1998–2005. [CrossRef]
33. Tychsen, J.; Rösler, J. Production and characterization of porous materials with customized acoustic and mechanical properties. In *Fundamentals of High Lift for Future Civil Aircraft*; Springer: Berlin/Heidelberg, Germany, 2021; pp. 497–512.
34. Tychsen, J.; Lippitz, N.; Rösler, J. Modification of porous aluminum by cold rolling for low-noise trailing edge applications. *Metals* **2018**, *8*, 598. [CrossRef]
35. Uphoff, S.; Krafczyk, M.; Kutscher, K.; Rurkowska, K.; Langer, S.; Lippitz, N.; Faßmann, B. A hierarchical approach to determining acoustic absorption properties of porous media combining pore-resolved and macroscopic models. *J. Porous Media* **2018**, *21*, 83–100. [CrossRef]
36. Kuschmitz, S.; Ring, T.P.; Watschke, H.; Langer, S.C.; Vietor, T. Design and Additive Manufacturing of Porous Sound Absorbers—A Machine-Learning Approach. *Materials* **2021**, *14*, 1747. [CrossRef] [PubMed]
37. Gao, N.; Wang, M.; Cheng, B.; Hou, H. Inverse design and experimental verification of an acoustic sink based on machine learning. *Appl. Acoust.* **2021**, *180*, 108153. [CrossRef]

38. Lähivaara, T.; Kärkkäinen, L.; Huttunen, J.M.; Hesthaven, J.S. Deep convolutional neural networks for estimating porous material parameters with ultrasound tomography. *J. Acoust. Soc. Am.* **2018**, *143*, 1148–1158. [CrossRef] [PubMed]
39. Jeon, J.H.; Yang, S.S.; Kang, Y.J. Estimation of sound absorption coefficient of layered fibrous material using artificial neural networks. *Appl. Acoust.* **2020**, *169*, 107476. [CrossRef]
40. Gardner, G.C.; O'Leary, M.E.; Hansen, S.; Sun, J. Neural networks for prediction of acoustical properties of polyurethane foams. *Appl. Acoust.* **2003**, *64*, 229–242. [CrossRef]
41. Ciaburro, G.; Iannace, G.; Puyana-Romero, V.; Trematerra, A. A comparison between numerical simulation models for the prediction of acoustic behavior of giant reeds shredded. *Appl. Sci.* **2020**, *10*, 6881. [CrossRef]
42. Casaburo, A.; Magliacano, D.; Petrone, G.; Franco, F.; de Rosa, S. Optimizing the acoustic properties of a meta-material using machine learning techniques. In Proceedings of the INTER-NOISE 2021—2021 International Congress and Exposition of Noise Control Engineering, Glasgow, Scotland, 21–24 August 2021.
43. Casaburo, A.; Magliacano, D.; Petrone, G.; Franco, F.; De Rosa, S. Gaussian-based machine learning algorithm for the design and characterization of a porous meta-material for acoustic applications. *Appl. Sci.* **2022**, *12*, 333. [CrossRef]
44. Xu, F.; Uszkoreit, H.; Du, Y.; Fan, W.; Zhao, D.; Zhu, J. Explainable AI: A brief survey on history, research areas, approaches and challenges. In Proceedings of the CCF International Conference on Natural Language Processing and Chinese Computing, Guilin, China, 24–25 September 2019; Springer: Berlin/Heidelberg, Germany, 2019; pp. 563–574.
45. Linardatos, P.; Papastefanopoulos, V.; Kotsiantis, S. Explainable ai: A review of machine learning interpretability methods. *Entropy* **2020**, *23*, 18. [CrossRef]
46. Došilović, F.K.; Brčić, M.; Hlupić, N. Explainable artificial intelligence: A survey. In Proceedings of the 2018 41st International Convention on Information and Communication Technology, Electronics and Microelectronics (MIPRO), Opatija, Croatia, 21–25 May 2018; IEEE: Piscataway, NJ, USA, 2018; pp. 0210–0215.
47. Samek, W.; Wiegand, T.; Müller, K.R. Explainable artificial intelligence: Understanding, visualizing and interpreting deep learning models. *arXiv* **2017**, arXiv:1708.08296.
48. Samek, W.; Müller, K.R. Towards explainable artificial intelligence. In *Explainable AI: Interpreting, Explaining and Visualizing Deep Learning*; Springer: Berlin/Heidelberg, Germany, 2019; pp. 5–22.
49. Ring, T.P.; Kuschmitz, S.; Vietor, T.; Langer, S.C. Design und Analyse generischer poröser Materialien mittels Machine-Learning Methoden. In *Proceedings of the Fortschritte der Akustik-DAGA 2021, Stuttgart, Germany, 21–24 March 2021*; Deutsche Gesellschaft für Akustik e.V.: Berlin, Germany, 2021.
50. ISO. *ISO 9053-2:2020*; Acoustics—Determination of Airflow Resistance—Part 2: Alternating Airflow Method. Technical Report. International Standardisation Organisation: Geneva, Switzerland, 2020.
51. ISO. *ISO 10534-2:1998-11*; Acoustics - Determination of Sound Absorption Coefficient and Impedance in Impedance Tubes—Part 2: Transfer-Function Method. Technical Report. International Standardisation Organisation: Geneva, Switzerland, 1998.
52. Carbajo, J.; Molina-Jordá, J.; Maiorano, L.; Fang, N. Sound absorption of macro-perforated additively manufactured media. *Appl. Acoust.* **2021**, *182*, 108204. [CrossRef]
53. Chollet, F. Keras. 2015. Available online: https://keras.io (accessed on 31 October 2022).
54. Saltelli, A.; Ratto, M.; Andres, T.; Campolongo, F.; Cariboni, J.; Gatelli, D.; Saisana, M.; Tarantola, S. *Global Sensitivity Analysis: The Primer*; John Wiley & Sons: Hoboken, NJ, USA, 2008.
55. Wong, F.S. First-order, second-moment methods. *Comput. Struct.* **1985**, *20*, 779–791. [CrossRef]
56. Saltelli, A. Making best use of model evaluations to compute sensitivity indices. *Comput. Phys. Commun.* **2002**, *145*, 280–297. [CrossRef]
57. Herman, J.; Usher, W. SALib: An open-source Python library for Sensitivity Analysis. *J. Open Source Softw.* **2017**, *2*. [CrossRef]
58. Bratley, P.; Fox, B.L. Algorithm 659: Implementing Sobol's quasirandom sequence generator. *Acm Trans. Math. Softw.* **1988**, *14*, 88–100. [CrossRef]
59. Matyka, M.; Koza, Z. How to calculate tortuosity easily? *Aip Conf. Proc.* **2012**, *1453*, 17–22. [CrossRef]
60. Lee, H.R.; Yang, S.S.; Lee, J.W.; Kang, Y.J. Estimation and uncertainty analysis of fluid-acoustic parameters of porous materials using microstructural properties. *J. Acoust. Soc. Am.* **2020**, *148*, 308–323. [CrossRef]
61. Perrot, C.; Chevillotte, F.; Panneton, R. Bottom-up approach for microstructure optimization of sound absorbing materials. *J. Acoust. Soc. Am.* **2008**, *124*, 940–948. [CrossRef]